Atom Probe Tomography for Biomaterials and Biomineralization Research

Kathryn Grandfield*[1,2,3], Chiara Micheletti[1], Joseph Deering[1], Gabriel Arcuri[4], Tengteng Tang[1], Brian Langelier[4]

[1] Department of Materials Science and Engineering, McMaster University, Canada
[2] School of Biomedical Engineering, McMaster University, Canada
[3] Brockhouse Institute for Materials Research, McMaster University, Canada
[4] Canadian Centre for Electron Microscopy, McMaster University, Canada

*Corresponding Author:
Department of Materials Science and Engineering
McMaster University
1280 Main Street West
Hamilton ON L8S 4L8 Canada
Email: kgrandfield@mcmaster.ca

Abstract
Natural and synthetic biomaterials are part of our daily lives, from our own skeleton and teeth to coral reefs and carbon-capturing single-cell organisms in the oceans, to engineered ceramics and minerals comprising our toothpaste and bone replacements. Many natural biomaterials are hierarchically structured with remarkable material properties that arise from their unique combination of organic and inorganic components. Such structural hierarchy is often formed and developed through a process of biomineralization. Many fundamental questions remain regarding mineralization in bones, teeth, biomaterials and at biointerfaces, partly due to the challenges in characterizing three-dimensional (3D) structure and chemical composition simultaneously at the nanometer scale. Atom probe tomography (APT) is a 3D characterization technique that combines both sub-nanometer spatial resolution and compositional sensitivity down to parts per million. While APT is well-established in application to conventional engineering materials, advances in recent years have seen its expansion into the field of biomineralization research. Here, we focus our review on APT applications to biominerals, biomaterials and biointerfaces, providing a high-level summary of the findings unveiled in biomineralization by APT, as well as a primer on its theory and best practices specific to the biomineralization community. We show that APT is a promising characterization tool already applied to some biomaterials, where its unique ability to quantify 3D chemical composition is not only complementary to other microscopy techniques but could become an integral part of biomaterial research. With the emerging trends of correlative and cryogenic analysis workflows, APT has the potential to improve fundamental understanding of a broader range of biomaterials, while deriving novel perspectives on clinical applications and strategies for functional material design.

1 Introduction

Biominerals are formed by living organisms through selective uptake of elements from the local environment that are then incorporated into hierarchically structured organic-inorganic materials under direct biological control, also referred to as biomineralization [1]. Biominerals have a vast presence in the biosphere, including environments such as coral reefs and limestone caves, and siliceous shells of algae and diatoms [2]. Consequently, they have a major impact on ocean chemistry, and ultimately global climate change. Among one of the most important functions of biominerals is to provide sufficient mechanical strength and toughness to the skeleton of organisms as they progressively adapt to their evolving environment [2]. Many natural biominerals therefore exhibit impressive mechanical properties that are far superior to their synthetic counterparts, largely due to their unique compositional character and structural organization [3].

In contrast to classical crystallization pathways, amorphous precursors and nanocrystals are commonly observed as building units during the formation and development of biominerals found in diverse structures (e.g., bone, teeth, coral skeletons, molluscan shells, sea urchin spines, etc.) [4,5]. Material scientists are engrossed by this unconventional process and captivated by the precise control organisms elicit over the composition, morphology, and architecture of biominerals. These unique properties enable their structure to fulfil multiple biological and mechanical functions which have propelled biomedical engineers to adapt strategies to develop synthetic biomaterials. Yet, the structures themselves, such as the vertebrate skeleton, often bring a multitude of health-related problems, such as bone fracture, mineral loss (i.e., osteolysis), dental caries, osteoporosis and more. Research on biominerals, thus, lies at the forefront in the development of new technologies relevant to all aspects of life, from fundamental material chemistry and environmental sciences to biomedical engineering and clinical applications. It is therefore evident that an in-depth understanding of the composition and structure of biominerals is essential to design strategies directed toward developing biomimetic and bioinspired materials for functional and therapeutic materials.

Current technologies for investigating the three-dimensional (3D) structure and composition of biominerals and their synthetically designed biomaterial counterparts are well-established at various length scales and volumes, each with distinct benefits and shortcomings, and are well summarized elsewhere [6–9]. With most of these techniques, a tradeoff usually exists between resolution and volume probed. Using a simplified model of bone's hierarchical structure, from building block components up to microscale osteons, we relate the volume and resolution of standard 3D imaging tools (Figure 1a) to these biological features (Figure 1b). Common analyses range from X-ray based micro-computed tomography (micro-CT) [10] which has the advantage of capturing micrometer scaled features, such as osteons and osteocytes, but lacks high resolution or detailed elemental information, to synchrotron-radiation tomography tools (SR nanoCT), which provide higher resolution on the range of nanometers [11]. Electron-based tools for 3D analysis include focused ion beam-scanning electron microscopy (FIB-SEM) serial sectioning or nanotomography [12] which provides nanometer clarity over tens of micrometers (e.g., covering several layers of bone lamellar tissue [13,14] and fine structural features such as canaliculi and mineral clustering [15–17]) while larger volumes can be obtained when using a plasma ion source [18]. In both cases, FIB-SEM has limited opportunities for quantitative elemental information unless coupled with spectroscopy. Similarly, transmission electron microscopy (TEM) which probes at higher resolution to view components such as collagen fibrils and nanoparticles has been used in electron tomography to provide 3D structural [19] and indirect chemical information (when comprised of images from high angle annular dark field detectors for compositional contrast) [20,21]. Scanning TEM (STEM) can be coupled with high resolution spectroscopic elemental mapping such as electron energy loss spectroscopy (EELS) or energy dispersive spectroscopy (EDS) to provide so-called four-dimensional (4D) tomography [22]. This can be even achieved at the atomic-scale; however this is largely prohibitive for beam-sensitive organic or non-conducting materials, leaving a gap in technologies to obtain chemical information at the sub-nanometer scale.

Atom probe tomography (APT) is an analytical microscopy technique that provides 3D mapping of nanoscale volumes with sub-nanometer spatial resolution and chemical sensitivity in the parts per million range (for a comprehensive technical review, see [23] and references therein). Placed in the context of other multidimensional characterization tools (Figure 1), this unique combination of 3D compositional data at sub-nanometer resolution fills a niche in the biomaterials characterization toolbox. It therefore stands to contribute greatly to the structural organization of biominerals and biomaterials, specifically at the level of building block components, such as collagen fibrils and hydroxyapatite (HA) crystals in natural tissue, or nanoparticles or trace-element inclusions in synthetic biomaterials, or nanoscale components at functional biointerfaces.

Initially, APT was developed in application to materials well suited to withstand the field evaporation process key to this technique. Metals and alloys could easily undergo ionization and desorption of atoms from their outermost surface given a sufficiently large electric field, driven by an applied voltage and small sample tip radius, which could be pulsed to trigger timed ionization events and enable time-of-flight measurements. Laser-assisted APT later emerged by coupling an atom probe microscope with a laser, and using a static electric field combined with laser pulses to produce field evaporation [7] thus expanding the envelope of suitable materials for APT to include semiconductors [24] and other electrically insulating materials. The application of APT to biominerals was first highlighted by Gordon and Joester who successfully characterized the chemically complex nanometer-scale interfaces in the tooth of a marine chiton [25]. This work has since paved the way for the broadening applications of APT to a growing range of natural biominerals, including bone [26,27], dental enamel [28–31], and carbonates from marine

organisms [26,32,33], biomaterials such as synthetic bioceramics and bioglasses [34,35], and biointerfaces [36].

In this review tailored to the biomaterials and biomineralization community, we introduce the fundamental concepts of APT from the lens of biomaterials applications. We provide a focused review on the applications of APT to biominerals, biomaterials, biointerfaces and biological matter to date, highlighting the structure-property or mechanistic insights offered by APT. We place special consideration on challenges, sample preparation strategies, and provide future perspectives to broaden APT use in the biological sciences.

2 APT Fundamentals

Presented below is a brief overview of APT as a technique. However, for a more thorough examination of the history, underlying physics, and analytical performance of APT, readers are directed to some of the many excellent texts already written on this topic [37–39].

The atom probe microscope evolved from the pioneering work of E.W. Müller who successfully imaged and resolved individual surface atoms through field evaporation with the field ion microscope (FIM) [40,41]. The combination of this field evaporation with the identification of individual ions using time-of-flight mass spectrometry gave rise to the first atom probe-field ion microscope (APFIM) [42] that has subsequently evolved to yield 3D imaging capabilities [43–45] and into the modern Local Electrode Atom Probe (LEAP) used today [46].

An APT experiment can be roughly divided into the stages of (i) data acquisition, (ii) reconstruction, and (iii) visualization and analysis, as shown schematically in Figure 2. Data acquisition is where a sample is destructively measured using the atom probe instrument. The reconstruction step converts the outputs of that measurement into a 3D model of the original material. Visualization and analysis examine that 3D model to uncover knowledge about the sample, while remaining aware of the influences, limitations, and potential artifacts linked to each of the previous stages. As the most appropriate visualization and analysis methods vary with each sample and scientific question, only the data acquisition and reconstruction stages are detailed in this section.

APT data acquisition involves the successive field evaporation of surface ions from a sample. Field evaporation itself is induced by a strong electric field [47], on the order of 10^{10} V/nm [38]. This field can be reached at the specimen surface under an applied voltage for samples shaped into the form of nanoscale needles (generally <100 nm radius at the apex), as the field strength is inversely proportional to the sample tip radius. The ability to produce specimens with tips of sufficient size for field evaporation is a critical step to APT analysis and is detailed further in Section 4.3. Ion identification depends on measuring the time-of-flight (ToF) following field evaporation, so the start time of such events must be controlled. To achieve this, the specimen surface is held close to the field required to ionize atoms from the surface and evaporation events are controlled by applying successive voltage or laser pulses that briefly expose the sample to conditions where the energy barrier for field evaporation is likely to be overcome. Evaporated ions are then accelerated by the electric field toward a position-sensitive (e.g., delay line) detector where the position (x, y) and timing of each ion impact is recorded. The data acquisition stage typically proceeds until a satisfactory number of ion counts (on the order of several million) have been registered, or successive evaporation and subsequent increase of the tip radius limits the applied electric field, or the sample prematurely fractures. Other requirements of data acquisition include an ultrahigh vacuum (order of 10^{-11} Torr) required to reduce background signal and an extremely low sample base temperature (typically 25-80 K) to limit uncontrolled atom movement or evaporation and improve spatial accuracy.

Reconstruction of the acquired data aims to both determine the chemical identity of each ion, and to assign to it a position in 3D space equivalent to its original position in the sample. The chemical identities of ions are determined by converting the ToF into a mass-to-charge ratio by equating it to their acquired kinetic and potential energies. A histogram of mass-to-charge data points, generally called a mass spectrum, is then produced with peaks representing elemental or molecular species at different charge states (e.g., +1, +2, +3) that are dependent on the element, phase, and the intensity of the electric field [48]. The chemical identity of each ion or molecule is assigned manually through a process referred to as mass peak ranging.

Spatial reconstruction to produce a 3D representation of the analyzed volume generally assumes a reverse-projection model and converts ion hit positions on the position-sensitive detector to real-space coordinates [49]. The lateral x- and y-positions of ions on the sample surface are determined by tracing the ion flight paths from the detector location back to the specimen surface. This process must account for the instantaneous magnification of the sample at the time of evaporation, and typically assumes the sample surface shape as a perfect hemispherical cap on a truncated cone with the radius of the cap blunting itself uniformly with each successive evaporation throughout the experiment. The depth (z-coordinate) of each ion is determined using a reverse sequence model of evaporation that is adjusted in increments that are proportional to the volume of each individual ion and must account for the limitations in efficiency of the atom probe instrument in detecting every evaporated ion [49]. Spatial calibration of the reconstruction is often aided with information on the sample size, tip shape, or structure, which can be provided by complementary imaging methods (e.g., SEM, TEM). The result is a data array representing a point cloud with each ion having a (x, y, z) position determined to accompany its mass-to-charge value. In combination with the mass peak ranging information, a 3D model of the original sample is produced.

As this review will highlight, this combination of high chemical sensitivity and spatial resolution makes APT well-suited for detection of trace elements or dopants within natural and synthetic biomaterials. This may aide in identification of clustering of atoms, as well as their clustering, e.g., grain boundary segregation in crystalline biomaterials, core-shell nanoparticle structures, or for delineating the boundaries between organic/inorganic regions in nanocomposites. Below, we give examples of these findings in the study of biominerals, such as bones, teeth or carbonates, biomaterials, biointerfaces, and other biological materials, including cells and proteins.

3 Applications in Biominerals, Biomaterials and Biointerfaces

3.1 Bones and Teeth

Many biological tissues can be viewed as nanofibrous composites that are structured hierarchically across different length scales [50]. Two such examples are bone and tooth. The basic constituents, mainly carbonated HA nanocrystals and collagen, assemble to form a complex hierarchical structure, from the individual collagen fibril and mineral nanoplatelets at the nanometer level, to the microscopic structural units of osteons and lamellae in bone and peri/intertubular dentin in tooth, to the macroscopic level of a trabecular core and cortical shell in bone and an enamel cap encompassing a mass of dentin in tooth [51–54].

The remarkable mechanical properties (e.g., hardness and toughness) and biological functions (e.g., calcium homeostasis) of bone and tooth are thought to arise from the adaptation of the structure at all length scales of the hierarchy [50]. Therefore, a clear understanding of their complex structure has a major impact for elucidating the structural-mechanical function

relationship and mechanisms of biomineralization. In recent years, many studies, with the help of the advances in imaging techniques and image processing algorithms, were able to visualize some refined structural features at the level of mineralized collagen fibrils in 3D and shed light on the structural hierarchy [15,18,21,55,56]. APT has added to this information by being uniquely positioned to probe the composition of mineral phases and trace elements within bones and teeth at relevant sub-nanometer length scales.

There have been, so far, only a few reports investigating mammalian bone using APT. The first published pilot study was conducted on rat femoral cortical bone by Gordon et al. where the spectra of the bone samples closely resembled that of the synthetic HA with Mg^{2+} and Na^{+} as substituents [57]. By combining scanning TEM (STEM) and APT, Langelier et al. examined human maxillary bone and showed a clear spatial correlation between inorganic mineral (Ca-rich) and organic matrix (C-rich) domains in mineralized collagen fibrils (Figure 3a) [58]. Further, the study demonstrated the capability of APT to detect trace elements (i.e., Mg and Na) and found co-localization of Na with organic-rich regions, and in amplified concentration at organic-inorganic boundaries, while Mg was confirmed within the mineral phase, suggesting the potential important role of Na in the structural integrity at the mineral-collagen interface. In recent work on leporine femoral lamellar bone, Lee et al. used APT to virtually extract individual mineralized collagen fibrils for analysis where the carbon isosurface visualization (Figure 2) showed a fibril-like helical structure, mirroring the collagen triple helix structure at the molecular level [59]. More importantly, the compositional and spatial sensitivity of APT enabled a clear separation of a single collagen fibril from the mineral (represented by Ca) and thus demonstrated that Ca (mineral) appeared both within and along/around the collagen fibrils (i.e., intra- and inter-fibrillar mineralization) with the majority of mineral concentrated in the external space between the fibrils (Figure 3b). Interestingly, by quantifying the atomic ratio between Ca and P (Ca/P) and their relative distance to collagen fibrils (C ions) via radial clustering analysis, the study found potentially greater quantities of amorphous calcium phosphorous (ACP) and/or poorly crystallized HA closer to and/or within the collagen fibril.

Compared to the few APT investigations on bone tissue, more work has been done on the mineralized tissues of the tooth, i.e., dentin and, especially, enamel, due to its lower organic content and, therefore, ease at which it runs in the atom probe. Gordon and Joester first reported that in the magnetite cap of chiton (marine mollusk) tooth organic fibers (mainly consisting of semi-crystalline α-chitin) were occluded throughout the tooth and co-localized with either Na or Mg ions, where Mg is a well-known element that modulates mineralization processes [25,60]. Interestingly, individual organic fibers had different chemical compositions (i.e., selective binding to either Na^{+} or Mg^{2+}), implying different functional roles in controlling fiber formation, mineral deposition, matrix-mineral interactions, and ultimately the mechanical properties of the tooth [25,60].

Similar to the chiton tooth, mature mammalian tooth consists of a softer core (dentin; collagen and HA) capped by a hard enamel layer (predominantly HA). In both rodent [28] and human enamel [30], APT has revealed an intergranular Mg-rich ACP phase between the HA nanowires that constitute the enamel structure (Figure 3c). Since Mg-rich ACP is more soluble than HA, the studies suggested that decay could occur via dissolution along the enamel rod boundaries and provided evidence for the potential strategies to strengthen (re-mineralize) enamel by introducing beneficial ions to the intergranular ACP. Such Mg segregation has likewise been reported in bovine enamel where the clustering of Mg had been associated with the changes in Ca/P ratio [61].

Gordon et al. also showed that in pigmented rodent enamel (a reddish-brown, iron-rich enamel), a mixture of ferrihydrite and an Fe-rich ACP phase replaced the Mg-rich ACP (Figure 3d), significantly improving not only its hardness (mechanical properties) but also the resistance to acid attack [28]. In a follow-up study on mouse enamel, Gordon et al. found elevated organic and carbonate content and possibly water at the ACP interphase which could further weaken the resistance to acid corrosion at the grain boundaries [29]. The authors also proposed that the mechanical behavior of the mouse enamel was attributed to the presence of the Mg-rich phase at the grain boundaries, rather than organic phases based on the observation of the absence of monolayer of organic matter surrounding individual crystallites [29]. More recent APT work combined with HAADF STEM on human enamel has revealed additional nanoscale pathways where dental decay/caries have been shown to progress including along the central dark line enriched with Na and Mg ions within carbonated apatite nanocrystals, in organic-rich precipitates, and at high-angle grain boundaries [31].

In the latest work by DeRocher et al., human premolars were examined with APT and correlative high resolution TEM imaging and EELS spectroscopy [62]. It was shown that Mg levels were elevated not only in the intergranular Mg-ACP, but also in two distinct layers in the core of crystallites which were further enriched in Na, F, and carbonate (Figure 3e). The crystalline core was surrounded by a shell with lower concentration of substitutional defects. This core-shell architecture led to a mechanical model predicting the residual stresses arising from the chemical gradients might affect the mechanical resilience of enamel. Based on the observations of the systematic variation in the concentration of Mg and other minor ions at the crystallite surface, the authors further proposed a mechanism for human enamel crystallite growth during amelogenesis (enamel formation) [62,63].

In contrast to enamel with little organic content (~ 1-2 wt%), dentin is a closer resemblance to bone because of its higher organic composition (~ 20 wt%). Gordon et al. first demonstrated in elephant tusk dentin that APT was able to reconstruct fibrous organic structures potentially corresponding to individual collagen microfibrils consisting of five collagen triple helices [57]. These fibrous structures were further found to co-localize with high Na concentrations and not with Mg ions, suggesting selective binding that may have impacts on collagen fibril self-assembly and/or functional properties of the tissue [57]. In another study on native pig dentin, Forien et al. discovered significant amounts of C residing within the mineralized Ca-rich domains (crystalline regions of the mineralized collagen fibrils) and there was a high inverse linear correlation between C and P [64]. Subsequently, the authors concluded that carbonate existed throughout the nanocrystals rather than being confined at the crystal boundaries, and it was of a B-type substitution where carbonate takes the place of phosphate in the HA crystal [64]. This work employed a common approach seen in the visualization of earlier mineralized tissues, specifically, separating the domains into mineral-rich and organic-rich/protein-rich regions. Mineral rich zones were identified as ≥ 34 at% Ca but protein-rich regions were denoted by ≥ 5.2 at% N, not as regions rich in C as used by other groups investigating bone [59]. Interestingly, this approach allowed for the interrogation of carbonate substitution, which was generally overlooked in the works on bone tissue.

APT has also been used to build an understanding of the superiority of some biominerals under mechanical loading. For example, in the ant mandibular tooth, APT revealed a homogeneous distribution of Zn, likely associated with residual proteins in the matrix, which provided improved mechanical properties over alternative strategies like inclusions that may lead to fracture [65]. This work also highlighted the importance correlative methods play in APT interpretation, where time-of-flight secondary ionization mass spectrometry (ToF-SIMS) was used to assist in mass peak ranging to understand potential fragmentation [65].

3.2 Biomaterials

Simultaneous collection of both composition and structure with sub-nanometer resolution also allows a thorough understanding of structure-property relationships of synthetic biomaterials. Here, we highlight the applications of APT to calcium phosphate-based ceramics, bioactive glasses, glass ceramics and composites. Metallic biomaterials are mentioned briefly but featured in Section 3.3 where they interface with bone tissue.

Among the various apatites and calcium phosphates, HA is closest to the mineral phase in mammalian hard tissues, mainly in a carbonate-substituted form [54], hence HA-based biomaterials are extensively studied in biomedical engineering. Owing to this interest, Gordon et al. used APT to examine different members of the apatite family, which due to their low Z (atomic number) composition and beam sensitivity, are challenging to examine with spectroscopic methods in STEM, i.e., EDS or EELS [57]. APT spectra of different synthetic apatites, i.e., fluorapatite, chlorapatite, and HA, displayed distinct spectral features attributable to each channel ion, thus providing a method to fingerprint the different apatites despite their highly similar structure and composition [57].

Nanoparticles of synthetic HA are increasingly used for other applications in medicine and dentistry [66,67], but thorough understating of their structure-function relationships is hindered by difficulties in determining their nanoscale organization. While such a task could be accomplished by APT, several issues remain in preparing nanoparticles into needle-shaped samples. Mosiman et al. demonstrated that APT samples of fluoridated HA nanoparticles can be obtained by first encapsulating them with Al_2O_3 (by atomic layer deposition) or Au (by sputter-coating) (Figure 4a). Interestingly, in this study, the encapsulation approach also dictated the APT operation mode, i.e., laser-assisted for the encapsulation with Al_2O_3, and voltage-pulsing for the encapsulation with Au [68]. The use of voltage-pulsing is particularly noteworthy, as the majority of APT studies on nonconductive biomaterials have been performed using laser-pulsing. However, in this case, and in similar analyses using laser-assisted APT, minor constituents of F were undetectable and Na only detectable when using Al_2O_3 encapsulation and laser-assisted APT. While encapsulation is certainly an option for obtaining APT data of HA, further coating optimization is needed to reach both stoichiometric values representative of the bulk and trace element detection [68].

Metoki et al. first exploited the analytical capabilities of APT to study an electrodeposited calcium phosphate coating, a clinically available surface modification strategy for bone implants, using Au as a model substrate. By comparing Ca/P ratios from their APT analysis to theoretical values, and by correlating APT and TEM, they determined that a mixture of phases was present on the Au substrate (Figure 4b). This mixture was composed of ACP, dibasic calcium phosphate dihydrate, and octacalcium phosphate, and was postulated to act as a transient precursor to HA [69].

Recently, Ren et al. paved the way to the use of APT for the analysis of another common class of materials employed in the biomineralization field, bioactive glasses. Both the preparation of APT samples with FIB and the APT experimental conditions were optimized for Sr-containing bioactive glass particles. Such optimization work led to a successful experiment rate of 90% without premature fracture for strontium-releasing bioactive glass-based scaffolds, yielding up to 25 million ions. This work has laid the foundation for investigating Sr release from biomaterials *in vivo* in the future.

Combining the properties of glasses and ceramics, glass-ceramic composites have become widespread materials in dentistry thanks to their excellent mechanical and biological properties,

together with a good aesthetic appearance [70,71]. The use of dopants is a common practice to control the microstructure and properties of ceramics, impacting their use in applications beyond the biomedical field. In this context, understanding the dopant segregation at the grain boundaries is paramount but complex to accomplish. In a Y-doped ZrO_2-SiO_2 glass-ceramic studied by Fu et al., the limited concentration of the dopant posed major challenges in the determination of its segregation behavior, and both STEM-EDX and STEM-EELS provided inconclusive information. Due to its chemical sensitivity, APT was able to detect Y both at ZrO_2 grain boundaries and at the ZrO_2/SiO_2 heterophase interface (Figure 4c), and also revealed the core-shell structure of the ZrO_2 nanocrystallites, where the core of ZrO_2 solid solution is surrounded by a thin Zr/Si interfacial layer [35].

In another composite material, a Ti-6Al-4V metal matrix nanocomposite containing Ag nanoparticles for antibacterial applications, APT uncovered that Ag was present not only as Ag-rich 10-20 nm particles, but also as elemental Ag forming a solid solution with the Ti-6Al-4V matrix, hence providing information on the synthesis method [72]. Precise assessment of the chemical and structural heterogeneities in a Si mesostructure for lipid-supported bioelectric interfaces was also accomplished with APT [73].

As biomaterials may be comprised of metals, ceramics, polymers, composites of these classes, or include nanomaterials, the application of APT to this field is as virtually infinite as the material combinations that exist. The studies reported in this section are only a few examples of the advantages offered by APT in examining structure-property relationships in biomaterials. For instance, more papers can be found in the literature where APT was used to characterize materials that may be employed as biomaterials, such as Ti-based materials [74–79] and self-assembled monolayers [80–83]. Although not used for biological applications in these papers, these could aid the development of APT-based characterization of similar biomaterial systems. Nonetheless, a detailed analysis of these studies is out of the scope for this review.

3.3 Biointerfaces

Beyond probing the structure and chemistry of biomaterials themselves, APT has also been extensively used for the investigation biointerfaces to evaluate candidate bone-implant materials. Osseointegration, defined as the “direct contact between living bone and implant” was first identified by optical microscopy at the microscale level [84]. When electron microscopy was later used to investigate bone-implant interfaces, it became clear that the bone-implant bonding occurs at a length scale beyond that resolvable by light, introducing the concept of “nano-osseointegration” [8,85,86]. Despite advances in the study of osseointegration at the nanoscale, probing the first few nanometers of the bone-implant interface remains challenging, and different descriptions of the ultrastructure of said interface can be found in the literature, as thoroughly reviewed in [87]. Having proven to be a valuable tool for the characterization of organic-inorganic interfaces in biominerals, including bone, APT can be an asset for researchers in the field of osseointegration, further extending the resolution of bone interfaces down to the atomic scale.

Karlsson et al. first used APT to analyze the interface between bone and a biomedical device, a titanium implant with a mesoporous titanium oxide coating for local drug delivery, placed in the rat tibia [36]. Their work showed that osseointegration entails an atomic continuity between bone and implant, and, specifically, that the direct contact between the implant surface (i.e., TiO) and bone occurs through a Ca-enriched layer of bone mineral, without a protein interlayer (Figure 4d) [36].

The inorganic nature of the bone-implant interface, rich in Ca, was confirmed by Sundell et al., who examined the osseointegration behavior of a Ti-based dental implant with a sand-blasted

acid etched surface, retrieved from the human jaw [88]. A similarly surface-modified Ti-6Al-4V ELI (extra-low interstitials) orthodontic mini-implant exhibited an interface composed of interdispersed Ca and TiO, but scarce C, hence suggesting that, at the atomic level, bone bonding to the implant surface occurs via its mineral components, without mediation by proteins [89].

The potential of APT for osseointegration studies was furthered by implementing a correlative workflow, combining APT with on-axis electron tomography and EELS tomography, to characterize bone-implant interfaces in 4D (i.e., 3D structural information *plus* chemistry) [22]. This correlative 4D tomographic analysis showed that a transitional biointerphase was present at the bone- laser-machined Ti implant interface, with clear concentrations gradients of both Ca and Ti. Ca and C were both present in direct contact with the nano-oxide at the implant surface (Figure 4e), and trace amounts of Mg and Na were also detected at this interface [22]. Unexpectedly, a small enrichment of N was noted between the Ti and the TiO surface layer of the implant, likely incorporated during laser ablation of the implant in ambient prior to implantation (Figure 4e). This was the first time that such N-rich layer was detected on the subsurface of a commercial dental implant, an observation made possible by the high sensitivity of APT. This exemplifies the role that APT can play in precisely characterizing the surface of implants for bone applications, assessing the presence of elements and compounds that could go undetected with other techniques, but may influence the performance of the implant.

3.4 Other Biominerals

Biogenic mineral phases encompass a diversity of single crystals, composites, and amorphous materials [2]. There are approximately 60 different types of biominerals that have been discovered across a broad phylogenetic range of life, the most common ones, including carbonates, phosphates, halides, sulfates, silica, iron oxides, manganese oxides, sulfides, citrates, and oxalates [2]. While bones and teeth were presented separately above, there are numerous other biominerals which have benefited from APT analysis, summarized here.

Exploiting the chemical sensitivity of APT, Arola et al. showed that the ionic substitution of apatite in the limiting layer of elasmoid scales varies for different fish species [90]. Specifically, when comparing APT spectra of scales from carp, tarpon and arapaima, traces of Na and Cl were detected in the carp scales only, while Mg was found in the tarpon scales. While specific trace elements were not identified for the arapaima, this species had an attenuated mass spectrum in the C^+ and Ca^{2+} regions compared to the carp and tarpon, which could be indicative of dissimilar energy absorption [90]. Overall, since substitutions in the apatite crystal structure alter several mineral properties, more work is needed to understand the origin (e.g., environmental) and implications of the different substitution observed in fish scales according to the species [90].

APT has also played a substantial role in the characterization of calcium carbonate-based biominerals. Branson et al. combined two-dimensional (2D) information from ToF-SIMS with 3D data from APT to probe the organic template, i.e., the primary organic sheet, embedded in the $CaCO_3$ shell of the *Orbulina universa*, a planktic foraminifera widely used to study past climate [32]. APT findings alone could not confirm that the organics present corresponded to the primary organic sheet, but correlation with ToF-SIMS analyses helped corroborating such correspondence, in turn highlighting the importance of APT as a part of broader multiscale or correlative characterization approaches [32]. The existence of a continuous, planar interface between organic and inorganic regions, marked by an abrupt variation in Ca, C, and H, was clear from the 3D volume visualized after APT data collection and reconstruction [32]. Compositional profiles (proxigrams) across the organic-inorganic interface revealed that the organic phase was enriched in both Mg and Na (Figure 5a), unveiling the chemical heterogeneity of the intraskeletal

environment, and suggesting that non-Ca^{2+} ions could also play a part in biomineralization, for example by altering the surface properties and in turn the interfacial energy of the organic template [32].

APT analyses of the calcite portion of the shell of the common blue mussel (*Mytilus edulis*) showed an opposite trend in the distribution of Na compared to what was observed in the foraminifera [32], as low concentrations of Na were found in the inter-crystalline organic matrix [26]. As Na appeared co-localized with the mineral phase or with the intra-crystalline organic phase in the mussel shell (Figure 5b) [26], and not associated with the organic phase as in the foraminifera [32], Na might play a different role in the biomineralization of these two distinct organisms. In the mussel shell, areas corresponding to the inter-crystalline organic phase were more concentrated in O and C compared to the calcite regions, especially showing an enrichment of at least 1 at% in O with respect to the surrounding mineral phase [26]. Interestingly, APT sample preparation and data acquisition for the mussel shell indicated a potential role of the crystallographic orientation of the sample in the quality of the APT data obtained. Sample orientation (i.e., either nearly perpendicular to the *c*-axis of the calcite or containing the {0001} plane of the calcite) affected the ease/difficulty of sample preparation in the FIB, and yielded a dissimilar total ion count and spectra quality [26]. Curiously, the ease of sample preparation was inversely related to the quality of the APT results, and samples with calcite oriented nearly perpendicularly performed superiorly [26]. This highlights the need for optimization of sample orientation for a given biomineral, as other minerals, such as bone, have shown differing findings [59].

The role of intra-crystalline organics in biominerals was investigated by Pérez-Huerta et al. by examining the organics occluded in individual calcite crystals synthesized in different ways, i.e., grown in presence of chitin hydrogel, both without and with yatalase (a chitinolytic enzyme) treatment at different concentrations, or in presence of chitin nanofibers [27]. By comparing APT mass spectra with those acquired for geological calcite in a previous study [91], 21 peaks characteristic of chitin were identified. Samples treated with yatalase also displayed peaks corresponding to S, validating the use of APT for the analysis of sulphated polysaccharides in biogenic biominerals [27]. APT reconstructions demonstrated that the synthesis method affected the morphology of the chitin-based organic occlusions in the calcite matrix. For growth in chitin hydrogel, these occlusions were in the form of discrete nanosized clusters, which coalesced into a linear structure, associated with Na, for growth in presence of chitin nanofibers [27]. In another study using similarly synthesized calcite crystals as in [27], APT results showed that the synthesis method, especially the presence and concentration of the chitinolytic enzyme (i.e., yatalase), also affected the distribution of chitin within the calcite crystal [92]. In absence of yatalase treatment, little signal corresponding to chitin was detected inside the calcium carbonate region but was mostly localized on the edge of the sample instead [92]. On the other hand, clusters of COH^+ and COH_2^+, representative of chitin, were incorporated within the calcite matrix both for synthesis with yatalase treatment, especially at higher concentration, and for growth in chitin nanofibers, demonstrating the potential of APT to help understanding how chitin and chitinolytic enzymes regulate crystal growth [92].

A polymorph of calcite, aragonite is the inorganic constituent of nacre, also known as mother of pearl. In nacre, aragonite grains are enclosed by organic sheets and contain nanosized organic inclusions. This heterogeneous nanostructure, combined with its non-conductivity, makes nacre a challenging material for APT analyses, with very uneven evaporation behavior due to the distribution of the organic and inorganic phases. Thanks to a thorough optimization of operating conditions, Eder et al. were able to complete several successful APT analyses of nacre [33]. In one dataset, part of the organic membrane surrounding the aragonite grains was visualized due

to the enrichment in C, H and Sr (incorporated during the pulse chase labeling) (Figure 5c). In the other samples examined, only organic inclusions, indicated by C and H-related peaks in the mass spectra, were detected [33].

3.5 Other Biological Materials

Although this review focuses predominantly on the application of APT to biomineralization, it would be remiss not to mention a few key advances in analyzing other biological materials, such as cells, proteins and bacterium. Compared to spectra from biominerals, peak ranging tends to be more difficult in these organic-rich materials due to overlap in the mass-to-charge ratios of evaporated complexes (CO^+, N_2^+, and $C_2H_4^+$ at 28 Da, for example). Adineh et al. investigated a network of fibrils present within drug-resistant *Acinetobacter baumannii* bacterial cells after fixation (Figure 6a) and noted peaks attributed to C, N, O, and H_2O throughout the intracellular domain and organic-rich vesicles using a pulsed voltage mode of data acquisition [93]. Comparison of drug-resistant and drug-susceptible bacteria with APT also showed differences in fibril structure within the cellular envelope and the presence of a unique phosphocholine fragment at 58 Da in drug-susceptible strains [93]. A follow-up APT study of graphene-encapsulated *Acinetobacter baumannii* with pulsed voltage mode showed clustering of CO within the bacterial cell envelope and a lack of phosphocholine indicating potential lipid damage [94]. Narayan et al. have also investigated cellular components with APT of plunge-frozen and sputter-coated HeLa cells, finding that specimen orientation during FIB preparation played a large role in stability [95]. Heterogeneous distribution of elements was partially observed within the cell, where negative correlations were observed between C and Na but other complexes such as carbonyls were homogenously distributed [95].

At the sub-cellular level, assessment of ferritin protein structures has been conducted with a wide range of sample preparation approaches. Solidified Type 1 ferritin was prepared for APT using room temperature FIB techniques, and, using a laser pulse energy of 1-10 pJ, Greene et al. presented a list of charged ion species that can be attributed to ferritin dispersed within dried salts of $CdCl_2$ and NaCl, although the core-shell structure wasn't readily visible and Fe^{2+} peaks are likely convoluted with organic species [96]. Clear reconstruction of the core-shell model of ferritin was achieved by Perea et al. using a resin-embedding prior to APT in lowicryl, a resin devoid of any N [97]. This work highlighted the presence of radial layers of phosphate and sodium in between the Fe-rich core ($^{56}Fe^+$) (Figure 6b) and outer C-rich shell [97]. Here, resin-embedded nanoparticles of Fe_3O_4 were used as a reference material for compositional controls and selection of laser wavelength was thought to play a role in suppressing alkanes in the resulting data [97]. More recently, APT following graphene encapsulation of liquid-ferritin mixtures has also isolated amino acid locations within the peptide shell by using clustering techniques to separate regions where carboxyls ($COOH^{3+}$) are in close proximity to amines (CNH_2^+ or CNH_3^+) using a 0.5 nm threshold [98].

Other studies featuring proteins have been performed in APT. Operating parameters were explored and optimized, particularly laser energy, to enable APT of air-dried beta amyloid fibrils after deposition onto pre-sharpened aluminum posts [99]. In all samples probed, organic-rich longitudinal structures were visible, but mass-resolution was not sufficient to identify S within methionine groups [99]. In another interesting application of APT to biological materials, APT was shown as a tool capable of investigating protein conformation. Sundell et al. demonstrated a structurally accurate APT reconstruction immunoglobulin (IgG) suspended in a silica sol-gel matrix [100]. Single proteins of IgG (Figure 6c) were visualized by examining the spatial location

of amino acids and carboxyl species (using CNH_2^+ and CO_2^+ as markers), allowing for direct visualization of the F_{ab} and F_c regions within immunoglobulin and the hinge region within the molecule [100]. Aggregations of IgG were also seen in the form of pentameric structures with outward-facing F_{ab} domains [100]. Where the mass-to-charge ratios of many molecular fragments from proteins have been identified in early models of a scanning atom probe [101,102], the extension to local electrode APT for identifying organization and spatio-chemical behavior of organic phases is a burgeoning field of interest. Collectively, these studies demonstrate the potential APT may hold for probing biological species and signatures, and as a tool for structural biology.

4 Technical Considerations for Biomaterials and Future Perspectives

4.1 Technique Limitations

The growing applications of APT to biomaterials (natural and synthetic) is pushing boundaries for the chemical and isotopic mapping that can be achieved at the 3D nanometer scale. However, this does not come without its challenges. APT has several limitations associated with both its spatial and mass resolution, well detailed in technical review papers elsewhere [23]. However, some of these limitations and sources of artifacts are especially applicable to biomaterials due to their inherent inhomogeneous and/or insulating nature. Here, we highlight a few of the limitations and artifacts to consider when using APT for biomineralization investigations.

4.1.1 Data Yield

Every APT experiment is dependent on yield, i.e., the number of atoms successfully field evaporated and detected before the end of the data acquisition, which can be used for reconstruction. Low yield caused by premature sample fracture under high field and low temperature acquisition conditions can hinder APT analysis of a number of materials. This is particularly problematic for biomaterials. The exact mechanisms for sample fracture vary, and are often impossible to investigate *postmortem*, which makes discerning a correct sample preparation and experimental process difficult. Nevertheless, it is known that samples which (i) require lower evaporation field and uniform evaporation conditions, (ii) contain few internal defects, and (iii) generally have stronger and more ductile properties, all tend to exhibit higher yield and be more resistant to fracture. However, many biomaterials fail to satisfy these conditions and instead contain a variety of phases with various evaporation characteristics, a host of internal interfaces and defects, and are often comprised of weak or brittle phases (relying on their composite structure at larger length scales for optimal mechanical properties).

Experimental parameters such as higher base temperature, higher laser energy, and lower target detection rate are generally accepted to promote greater yield but can come with trade-offs in spatial resolution or spectral performance. The trade-offs between data quality and yield are important considerations for heterogenous biomineralized tissues, such as bone [58], and thermally insulating biomaterials such as bioglasses [34], or even more brittle tissue such as ashed dentin [64] which have been reported to fracture frequently during APT analyses. A more detailed review of fracture and yield would need to focus on particular samples, as the root issues are often as varied as the samples themselves, yet the challenge of obtaining acceptable data yield should always be considered when contemplating any APT study on biominerals and biomaterials. In Table 1, we give the reported values for operating parameters of the materials featured in this review in hopes that they serve as a starting point for future applications in this field. While there are some trends present, it is clear that they are highly sample dependent. Sample preparation considerations which can affect yield are discussed in Section 4.2.

4.1.2 Sample Heterogeneity and Inhomogeneous Evaporation

The heterogeneous composite structure of many biominerals, containing organic and inorganic (mineral) regions, can complicate APT analysis by causing inhomogeneous field evaporation from the sample surface. For example, an organic matrix and inorganic mineral or biointerface, are likely to require different conditions to induce field evaporation due to the different elements and types of bonding present in each phase. Barring rare cases where these differences are minimal, an APT specimen containing two phases of varying evaporation characteristics will result in preferential evaporation of the so-called 'low-field' phase relative to the 'high-field' constituents. Inhomogeneous field evaporation such as this can produce irregularities in the surface topography of the specimen, causing deviation from an ideal hemispherical cap. In turn, these irregularities affect the shape of the electric field emanating from the tip, and therefore the trajectories of the departing ions. Such ion trajectory aberrations, also known as "local magnification" effects [103], illustrated schematically in Figure 7a, can impact both the spatial and spectral fidelity of APT data. Artifacts created in the 3D reconstruction from such aberrations are difficult to correct and represent an important limitation when reporting the spatial resolution of a feature of interest as well as the composition of fine features or at interfaces.

Similarly, gradients in the electrostatic field or temperature at the surface of a sample may enable surface migration of atoms before desorption from the surface. This would result in the evaporation of ions from positions that are traced back to a site close to, but not exactly their original site in the material. An attempt to reconcile these challenges can be made via correlation with other high resolution imaging techniques, such as TEM or even electron tomography, which can be used to help guide a more accurate reconstruction (e.g., [22,64,104]). Comparing data with field evaporation simulations can also help identify the impact of such aberrations. However, the complexity of most biominerals and biointerfaces, or similarly composed biomaterials, precludes such an approach. Overall, these effects are largely accepted as tolerable sources of potential error in the biomaterials APT community.

4.1.3 Spectral Resolution and Sensitivity

An overwhelming majority of biominerals and biomaterials, with the obvious exception of metallic biomaterials, require laser pulsing to achieve yield in APT experiments due to their electrically insulating nature. Yet the poor thermal conductivity of these materials also adversely affects data quality. This is primarily due to heat retention following the applied laser pulse, as the specimen tip is relatively slow to cool. As the tip temperature remains elevated, with a slow decrease following the laser pulse, so does the probability of field evaporation. Therefore, the timing of evaporation for the departing ion may substantially lag behind the incidence of the pulse, causing an artificially lengthened ToF to be recorded. This appears in an APT mass spectrum as so-called 'thermal tails', trailing from peaks to higher values of mass-to-charge. Thermal tails can lead to a reduction in mass resolution as smaller peaks (e.g., minor and trace elements or lower abundance isotopes) are obscured by the increase they cause in the local background where they are located (Figure 7b). Adjustments in the laser pulse energy may have a positive impact on peak tails, as observed in some inorganic minerals (e.g., [105,106]), while adjustments to the base temperature will result in maximum heat flow rates out of the sample apex, but come with a trade-off of specimen yield, which is limited by the mechanical strength of the specimen.

The formation of molecular species during an APT experiment can also complicate the mass spectrum by forming a number of peak overlaps with single-ion species. Simple peak overlaps may be deconvoluted using natural isotopic abundances to determine the portion of each overlapping species [107].

4.2 Sample Preparation Considerations

As in all cases of APT sample preparation, the methods used to produce quality samples can have dramatic effects on data quality and yield. For both natural and synthetic biomaterials, which often suffer from poor data quality and yield in most cases, proper sample preparation is even more vital for success.

For most biominerals and some biomaterials, as well as biointerfaces, the heterogeneous structures and often fine-scale regions of interest targeted for analysis commonly necessitate use of a dual-beam FIB-SEM to produce samples. Among FIB techniques for sample preparation, the most common is that of the *ex-situ* lift-out [92–94], as outlined schematically in Figure 8a. This method involves localized gas ion deposition of a protective strip over the region of interest (often using Pt or W) which is cut out into a rectangular wedge using the FIB (most commonly a Ga liquid metal ion or Xe plasma source). Using a micromanipulator, the wedge is removed from the sample and cut into ~2 μm wide segments that are mounted on pre-sharpened posts, again using a gas ion deposition system. These posts can be prefabricated on Si coupons, electropolished metallic wires (e.g., W), or on portions of TEM half-grids (Figure 8b), depending on the needs for correlative TEM analyses. Each of the segments are then milled into conical needle-shaped pillars using a series of annular milling patterns with decreasing inner radii, and typically lower beam currents. A final milling step can be performed with a low voltage FIB (e.g. 2, 5, or 10 kV), which acts similar to broad-beam ion milling in removing regions of material damaged by ion implantation [108], and providing the last step of sharpening to produce a sample with an apex radius of less than 100 nm, as required to achieve successive and controlled evaporation (e.g., [109–111]). In some cases, nano biomaterials may also be encapsulated first and then FIB milled to the appropriate size (Figure 8d), or in the case of very small nanoparticles or proteins, applied directly to a presharpened tip (Figure 8e).

Biological materials may often have lower dose thresholds for beam damage than conventional materials. Therefore, reducing FIB-induced damage imparted by both the electron and ion beams is even more critical. For example, in the case of nacre, aragonite grains were found bending away from electron beam during FIB milling [33]. Lower electron beam voltage, ion beam voltage and ion beam currents have been used to such purposes in inorganic [34] and organic [48] materials. These are necessary considerations for maintaining the integrity of such materials.

When dealing with samples of interfaces between materials with very different field evaporation behavior, the relative position of the two materials and the orientation of the interface in the APT samples should be considered. In such cases, it is desirable that the lower field material can be evaporated first, rather than risk fracture by having high field material above it. For example, Sundell et al. concluded that samples of bone interfacing a Ti implant should be prepared such that the analysis runs first through the bone and then into the implant [88]. This resulted in higher data yields and better accounted for thermal tails, in turn eliminating artifacts such as apparent Ti signal in bone from mass spectra overlaps [88]. The same orientation was used successfully in Wang et al. [22].

In the case of biological tissues, improvements in sample preparation may lie even before the FIB step, such as in the preparation/collection of the ‘bulk’ tissue sample itself. For example, Kim et al. suggested that bone-implant interfaces can be better preserved by preparing the retrieved tissue-implant using cryofixation [89], as opposed to more conventional methods involving fixation, dehydration and resin embedding. This proved to be an effective strategy to prepare samples for subsequent FIB annular milling, while limiting the artifacts introduced [89]. Moreover, the orientation of heterogenous tissues may impact the success rate of APT experiments, where Lee et al. discovered that orienting the collagen fibrils (and therefore HA mineral) in bone parallel

to the long axis of the APT pillar [59] resulted in much lower instances of fracture and larger number of ions collected per experiment compared to their earlier work without preferred collagen orientation [58]. Based on the HAADF-STEM images presented in Forien et al. prior to APT analysis, their samples of dentin similarly had HA crystals oriented more closely to the axis of the APT pillar than transversely to it, although the effect of this on the APT success rate is not commented on explicitly in this work [64]. There is potential that as in the natural tissue, for orientations along the length of the pillar, collagen fibrils provide additional mechanical integrity to survive the forces experienced during APT thermal and electric pulsing.

An additional consideration in the sample preparation workflow is the effect of coating the APT pillar following final sharpening. It has been claimed that conductive coatings have the potential to improve field evaporation of non-conductive specimens. For example, improved mass resolution and sample yield resulted when multi-layer Ag/Pd coatings were applied to conical pillars of SiN [112]. This methodology is not yet widely employed for biological materials and biointerfaces and has only explored by some. Wang et al. applied 15 nm of Ag by sputter coating to bone-implant APT specimens prior to APT, but due to the low sample yield, the effect of coatings was not studied or reported systematically [22]. The success of the coating material is also highly dependent on its adhesion to the underlying material. New strategies using single or multiple layers of graphene coatings have been demonstrated and show promise for future biological applications [113].

4.3 Future Directions and Opportunities Towards Biological Materials

Since biomaterials present additional challenges for data acquisition and reconstruction, due to their potentially non-conductive and heterogenous nature causing the limitations outlined above, there are several paths forward for increasing the efficacy of this tool in the biomineralization and related biomaterials community.

Firstly, APT holds great promise as a correlative tool, employed with other characterization methods that provide the necessary *a priori* information to improve the accuracy of APT reconstructions and visualizations. This has already been a hallmark of many APT studies included in this review where APT complements or correlates directly to other analyses by ToF-SIMS [65], (S)TEM [64], or EELS [22,62]. Implementation of APT into correlative workflows therefore holds great promise for expansion in the biomineralization field.

To further APT as a standalone characterization platform, improvements in mass ranging of complex molecular species are needed, particularly for organic phases. A better understanding of molecular ion fragmentation, if not possible to solve during acquisition, should be investigated with data processing means.

Increasing the throughput of the analysis of biological materials and some biomaterials may be influenced at the sample preparation stage. In-place or in situ APT [111] has not been implemented widely for biological materials and biomaterials, yet with the prevalence of Xe-based plasma FIBs increasing in laboratories worldwide, this may become an option for fast bulk milling and APT of regions of interest (shown in Figure 8c) without lift-out. However, the studies reviewed herein have emphasized the necessity to continue employing low electron and ion beam conditions to reduce sample damage.

Lastly, the future of APT of biological samples must certainly account for organic phases. This necessitates preserving the biological features, achievable with cryogenic freezing in vitreous ice to avoid the introduction of ice crystals and concomitant increase in volume. It would seem that the best path forward is the implementation of cryo-APT, for which several groups are working on

cryo-transfer platforms [114–117]. Several recent reviews comment more thoroughly on the advances in cryo-APT of biologics and liquids [118–120]. Implementation of cryo-APT would not only enable more biological materials, but a broader range of synthetic biomaterials, to be analyzed, though surely with increasing technical challenges.

5 Conclusion

APT combines both high spatial resolution and sensitive element detection in 3D, and therefore presents a characterization pairing hard to come by in the biomineralization toolbox. Although the inhomogeneous nature of some biological materials and biomaterials makes them inherently susceptible to challenges during APT analysis and interpretation, improvements in APT hardware, such as laser-assisted evaporation, have made it possible to analyze these materials. Herein, we summarized how APT has been used across a number of mineralized tissues, including dentin, enamel and bone, biomaterials, such as HA, bioactive glasses, and glass-ceramics, and at bone-implant interfaces and biological materials, such as cells and proteins. These studies provide a strong foundation to support expanding applications in the biomineralization and biomaterials field. Ongoing developments towards correlative workflows and cryo-APT will certainly widen future applications towards more organic and biological materials in the future.

6 Acknowledgements

The authors gratefully acknowledge funding support from the Natural Sciences and Engineering Research Council of Canada (NSERC) Discovery Grant and Canada Research Chairs Programs, where K.G. holds the Canada Research Chair in Microscopy of Biomaterials and Biointerfaces. G.A. and B.L are supported by the Canadian Centre for Electron Microscopy, a Canada Foundation for Innovation Major Science Initiatives funded facility (also supported by NSERC and other government agencies).

7 Author Contributions

Conceptualization: K.G.; Writing – Initial drafts, editing and approving final manuscript: All authors.; Funding acquisition and supervision: K.G.

Figures & Figure Captions

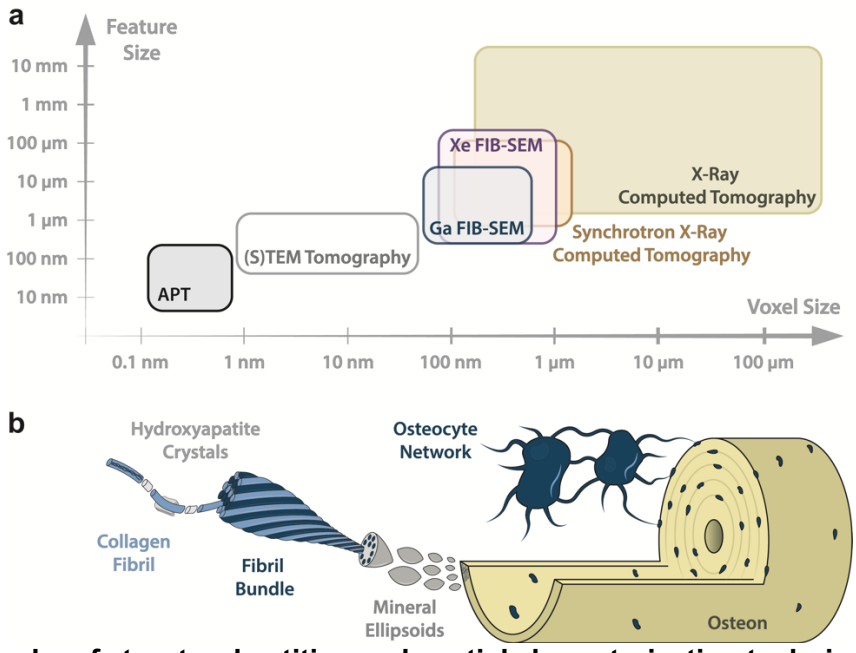

Figure 1. Hierarchy of structural entities and spatial characterization techniques in the field of biomineralization. a. X-ray computed tomography, focused ion beam microscopy (FIB-SEM), transmission electron microscopy (TEM), and atom probe tomography (APT) techniques fill different niches for 3D imaging of mineralized tissues and biointerfaces with respect to sample size and resolution. **b.** Matched to the hierarchically ordered structure of bone, features span from the microscale osteonal level to atomic features smaller than that a single collagen fibril. This necessitates the use of different analytical techniques for complete 3D mapping of structural features.

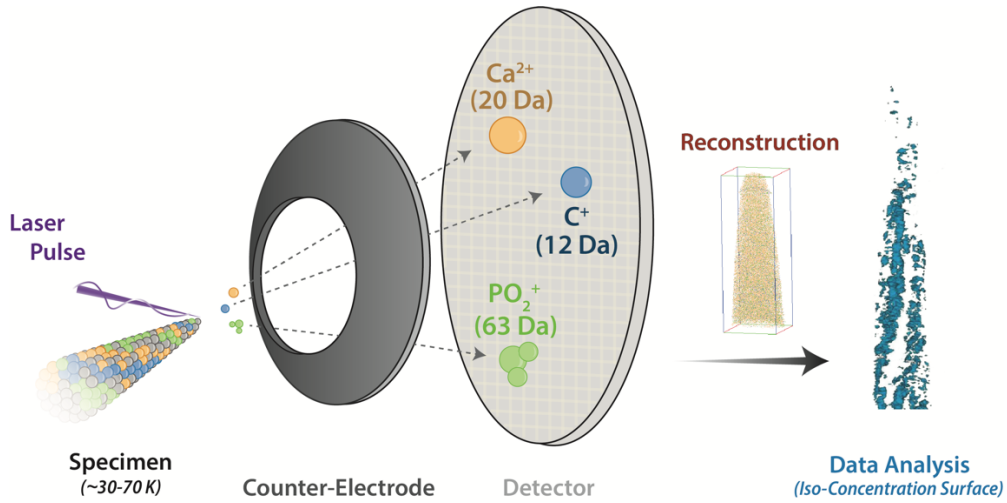

Figure 2. Operating principles of laser-pulsed APT. Field evaporation of charged atoms or complexes at the apex of a needle-shaped specimen is induced by an incident laser pulse, where species traverse the counter-electrode and impact the detector. The impact location on the detector is influenced by the mass-to-charge ratio of the ion/complex and can be matched with the precise timing of the laser pulse to map the origin of a single ion, which can then be represented by different visualizations, including the iso-concentration surface of carbon in bone shown here (partially adapted from [59] with permission from John Wiley and Sons).

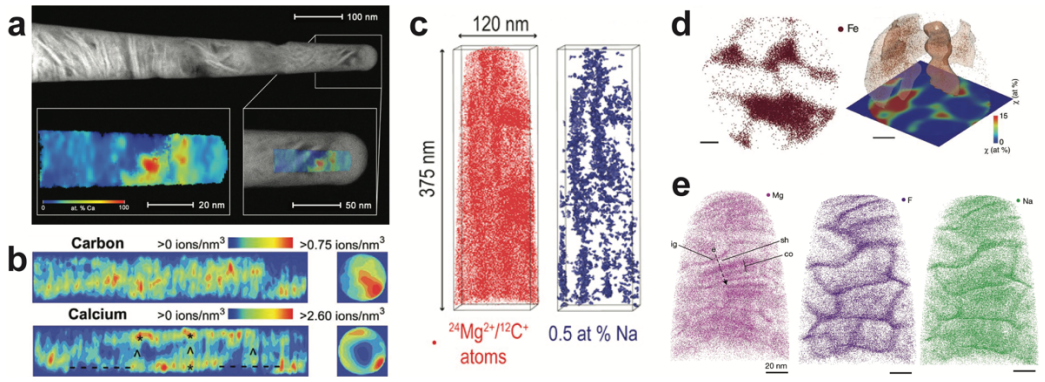

Figure 3. APT applications in bones and teeth. Correlative electron microscopy and APT reveal structural and chemical distributions in human bone, from [58] with permission from Springer Nature. **b.** Point density maps obtained from APT measurement of a collagen fibril showing distinct phases of C, representing collagen, and Ca, denoting mineral, predominantly exterior to but also infiltrating the collagen fibril, from [59] with permission from John Wiley and Sons. **c.** APT 3D reconstruction of human dental enamel illustrating a Mg-rich ACP phase and organic matter within HA nanowires, also high in Na content, from [30] with permission from AAAS. **d.** APT reconstruction of Fe ion position (left) and isosurfaces (right) showing its segregation to grain boundaries in pigmented rodent enamel, from [28] with permission from AAAS. **e.** APT rendering of Mg, Na, and F gradients in fluoridated human enamel crystallites, showing not only an intergranular increase in Mg-rich ACP, but two layers in the core enriched, forming a core(co) – shell(sh) architecture, from [62] with permission from Springer Nature.

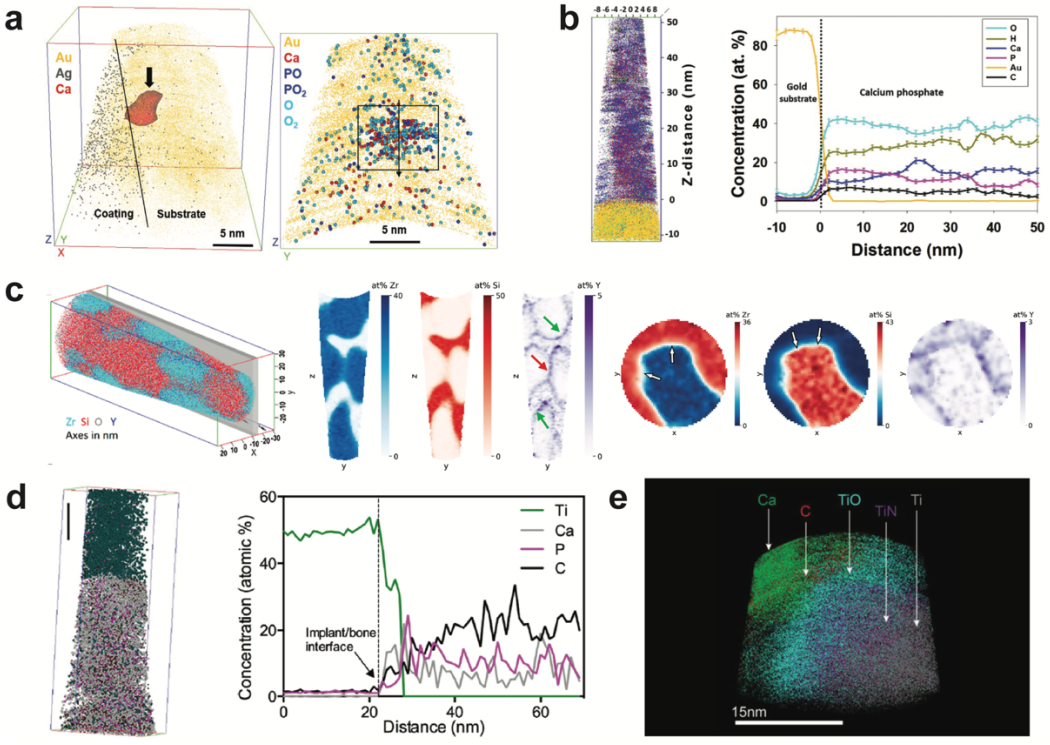

Figure 4. APT applications in biomaterials and biointerfaces. a. 3D visualization (left) and 2D slice along a representative yz plane (right) of a HA nanoparticle (Ca signal, red) encapsulated in Au (yellow), from [68] with permission from John Wiley and Sons. **b.** APT reconstruction (left) of

an electrodeposited calcium phosphate coating (blue/pink) on Au (yellow) and one-dimensional (1D) concentration profile along the z-axis (right), from [69] with permission from The Royal Society of Chemistry (CC-BY license). **c.** 3D reconstruction (left) of a glass-ceramic showing ZrO_2 nanocrystallites (cyan) in a SiO_2 matrix (red), with 2D contour plots along yz (middle) and xy (right) showing interfacial segregation of Y (purple), from [35] with permission from American Chemical Society. **d.** 3D reconstruction (left) of the interface between bone (grey and pink) and a Ti implant (green) and 1D concentration profile (right) across the interface showing a Ca-rich layer at the implant surface, from [36] with permission from American Chemical Society. **e.** 3D reconstruction of the the interface between bone (Ca and C, green and red, respectively) and a Ti implant (Ti, grey) showing a region containing N (TiN, purple) between the Ti implant and the implant surface oxide (TiO, cyan), from [22] with permission from John Wiley and Sons.

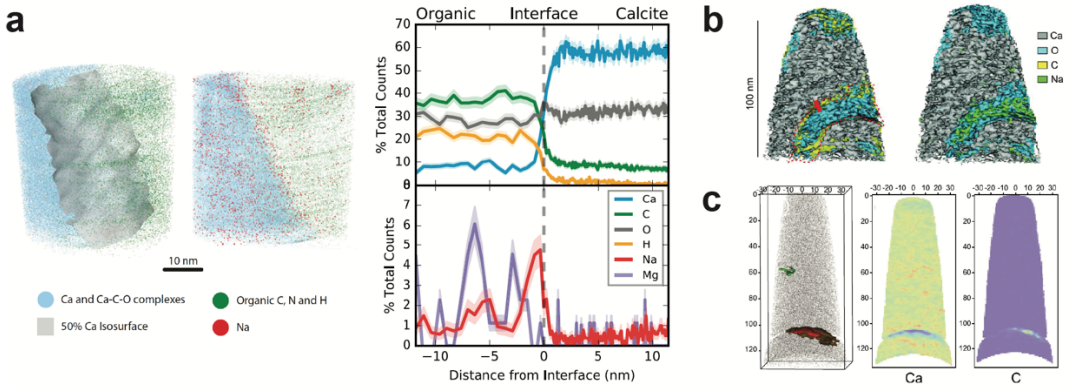

Figure 5. APT applications in carbonate biominerals. a. 3D reconstruction (left) of the interface between calcite (Ca-rich, light blue) and an organic region (Ca-poor, green) in the planktic foraminifera *Orbulina universa*, with proxigrams (right) across the interface highlighting an increase in Na (red) and Mg (purple) in the organic region, from [32] with permission from PNAS. **b.** 3D visualization based on elemental isoconcentration showing an organic-rich region (O and C, cyan and yellow, respectively) interfacing with calcite (Ca, grey) in a mussel shell, from [26] with permission from MDPI. **c.** 3D reconstruction (left) of the organic membrane (red) within nacre (Ca-rich, grey), and 2D slices (right) highlighting a depletion in Ca and an enrichment in C in correspondence with such membrane, from [33] with permission from John Wiley and Sons.

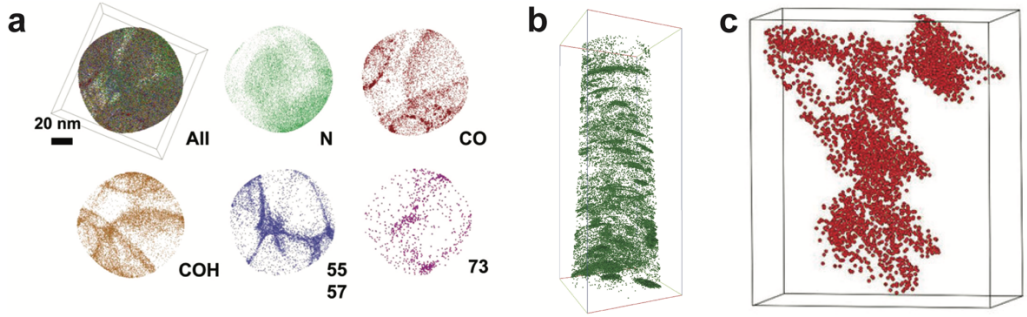

Figure 6. APT applications in other biological materials. a. APT reconstruction showing ion species present within the cell envelope of an antibiotic-resistant *A. baumannii* strain, from [93]

with permission from the American Chemical Society. **b.** Reconstructed volume of Fe distribution within resin-embedded ferritin, from [97] with permission from Springer Nature. **C.** Clustering analysis of CNH_2^+ and $CO2^+$ species within a single immunoglobulin molecule highlight the structure of the protein, from [100] with permission from John Wiley and Sons.

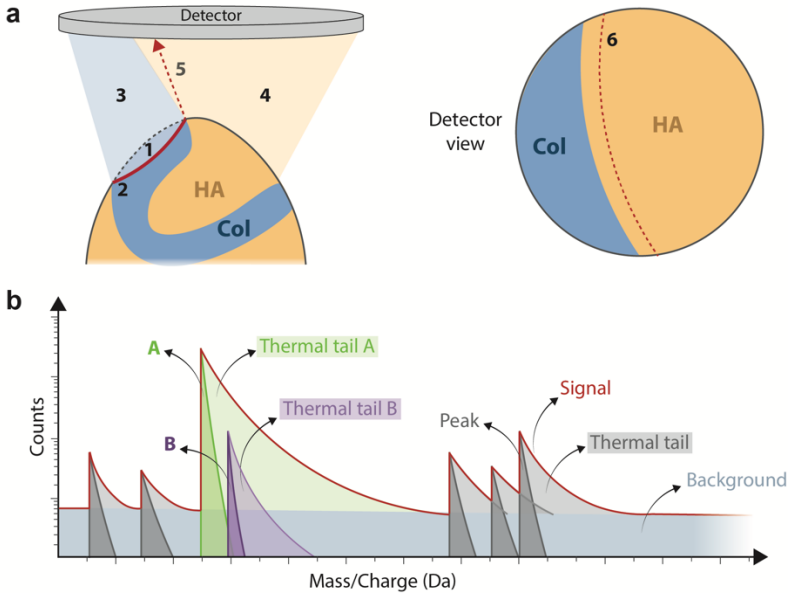

Figure 7. Common APT artifacts for biominerals and biointerfaces. a. The presence of uneven evaporation fields due to the inorganic (represented by hydroxyapatite, indicated as "HA", in orange) and organic (represented by collagen, indicated as "Col", in blue) phases in biominerals (exemplified by bone in this schematic) leads to the preferential evaporation of the low-field phase (no.1, faded blue region). This creates local topography on the tip which deviates from an ideal hemispherical shape (no. 2, red line), which in turn affects the electric field coming from the tip and the flight path of departing ions. These trajectory aberrations can result in so-called local magnification of phases, with low-field and high-field elements assuming a convergent (no. 3) and divergent (no. 4) evaporation trajectory with respect to the ideal trajectory in absence of magnification effects (no. 5, dashed red arrow). As a result, the low-field phase will appear smaller than its actual size, while the high-field phase will appear bigger than its actual size, as can be seen from the detector view (right side of image) by comparing the extension of each phase with respect to the interface in absence of aberrations (no. 6, dashed red line). **b.** Poor thermal conductivity of biominerals results in delayed cooling following laser illumination and extended ion departure time, which creates so-called thermal tails following the main ion peaks in the mass spectrum. Similar to uncertainties caused by peak overlap, such thermal tails can mask other peaks at slightly higher mass-to-charge ratios thereby reducing the mass sensitivity in those ranges. This effect hinders correct ion assignment and compositional accuracy and can produce compositional artifacts in multi-phase data. In the example shown in the schematic, the thermal tail following the peak of a certain species "A" (in green) covers the peak of species "B" (in purple).

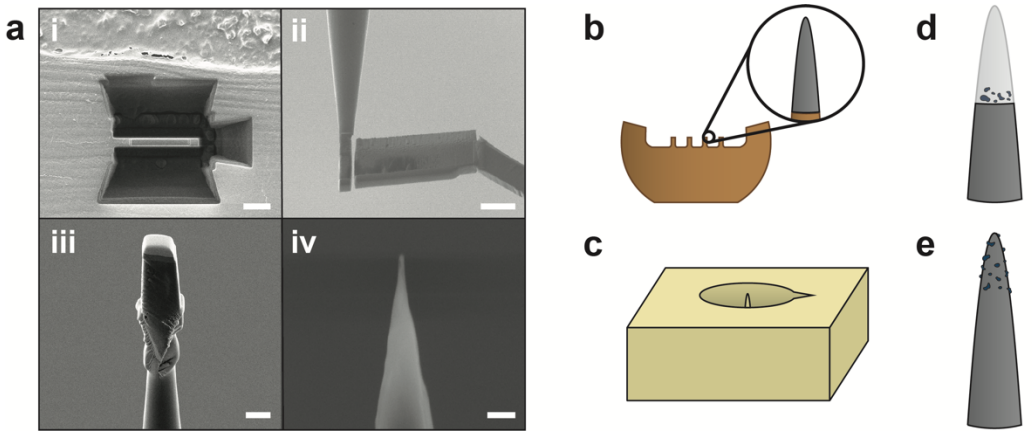

Figure 8. APT sample preparation strategies for biomaterials. a. Most samples are prepared in a dual-beam FIB-SEM, where trenches are milled around the ROI protected with capping layer (i). A rectangular wedge is removed using a micromanipulator (ii), cut into smaller segments, and attached to an APT post (iii). A needle-shaped sample with an apex radius smaller than 100 nm is finally obtained by annular milling (iv). Scale bars: i) 10 µm, ii) 5 µm , iii) 2 µm, iv) 200 nm. **b.** For correlative analyses, the wedge lift-out from a(ii) can also be mounted and thinned on the end of a TEM half-grid. **c**. In situ or in place APT preparation using a Xe FIB sharpens the sample directly in the bulk after using high ion beam currents to mill a large (~200 µm) hole around the site of interest. Lastly, nanoparticles or proteins can be prepared for APT by either **d.** encapsulation methods with sputter coated, atomic-layer deposition or sol-gel coatings followed by FIB sharpening, or by **e.** directly adhering to a pre-sharpened tip.

Table 1. APT operating parameters of various biominerals, biomaterials and biointerfaces.

Sample	Base Temp. (K)	Voltage or Laser [V/L-λ (nm)]	Pulse Frequency (kHz)	Pulse Energy (pJ)	Target Detection (Evaporation) Rate (% of pulses)	Ref
Bones						
Human maxilla*	43	L-355	160	75, 90	0.5%	[58]
Leporine femur	59.6	L-355	125	50	0.5%	[59]
Murine femur	40	L-355	200	150	0.25%, 0.5%	[57]
Teeth						
Human molar enamel	50	L-355	250	100	-	[30]
Human molar/premolar enamel	40	L-355	100	20	0.5 – 1%	[31]
Human premolar enamel	25	L-355	250	40	0.5%	[62]
Elephant tusk dentin	50	L-355	200	150	0.25%, 0.5%	[57]
Bovine incisor enamel	35	L	100-125	100	0.5%	[61]
Anterior porcine dentin	30	L-355	100	10	1.5%	[64]
Murine incisor enamel	40	L-355	200-250	50 -150	0.25%, 0.5%	[29]
Chiton tooth	40, 60	L-355	160-500	40 -75	0.25%, 0.5%	[25]
Ant mandibular tooth	30	L-355	100, 200	10 -100	-	[65]
Biomaterials						
Sr-bioactive glass*	30	L	200	200-250	0.3%	[34]
ZrO_2/SiO_2 glass ceramic	60	L-355	200	150-175	0.3%	[35]
Mesostructured silicon	30	L-355	250	30	-	[73]
Electrodeposited calcium phosphate	40	L-355	200	150	1%	[69]
Hydroxyapatite nanoparticles	50	V, L	200, 100	60	0.5%	[68]
Ti-5Al-5Mo-5V-3Cr alloy	40	L-355, L-512	-	50, 200	-	[75]
Ti-5Al-5Mo-5V-3Cr alloy*	30-45	L-532, L-355	-	10	-	[78]
Ti-1Al-8V-5Fe alloy	60	L-355	-	20	0.5%	[76]
Ti-6Al-4V and F1E alloys	40-55	L-535	200	200-400	-	[79]
Biointerfaces						
Bone-implant (human jaw)	30	L-532	100	300-500	-	[88]
Bone-implant (human mandible)	64.8	L-355	160	200	0.3%	[89]
Bone-implant (human maxilla)	43.4	L-355	100	120	0.5%	[22]
Bone-implant (murine tibia)	40	L-532	200	500	0.2%	[36]
Other Biominerals						
Foraminifera carbonate	44	L-355	160-200	50	-	[32]
Mussel shell calcite	40, 50	L-355	200	50, 500	0.2-0.5%	[26]
Mussel nacre	38-51	L-355	160-200	50-200	-	[33]
Chitin nanofibres	40	L-355	200	50	0.2-0.3%	[27]
Geological calcite and dolomite	50	L	-	150-1300	2%	[91]
Other Biological Materials						
Acinetobacter baumannii cells	60	V	200	-	0.5%	[93]
Acinetobacter baumannii cells	60	V	200	-	0.5%	[94]
HeLa cells	30	L-532	200	200-500	0.5-1%	[95]
Beta amyloid fibrils	50	L	125-500	10-40	0.2%	[99]
Ferritin	< 20	L-532	10, 100, 250	10-100	0.5%	[96]
Ferritin	44.1	L-355	160	0.2-400	0.2-0.3%	[97]
Ferritin	35	L	200	20	-	[98]
Immunoglobulin	30, 50	L-532	100-200	250-500	0.25-0.5%	[100]

* Optimized conditions reported here from a range presented in the article.

8 References

[1] S. Mann, Biomineralization: Principles and Concepts in Bioinorganic Materials Chemistry, Oxford University Press, New York, 2001.

[2] H.A. Lowenstam, S. Weiner, On Biomineralization, Oxford University Press, New York, 1989.

[3] F.C. Meldrum, Biomineralisation processes, in: P. Vadgama (Ed.), 1st ed., Woodhead Publishing, Boca Raton, Boston, New York, Washington DC, 2005: p. 824.

[4] M. Jehannin, A. Rao, H. Cölfen, New Horizons of Nonclassical Crystallization, J Am Chem Soc. 141 (2019) 10120–10136.

[5] J.J.D. Yoreo, P.U.P.A. Gilbert, N.A.J.M. Sommerdijk, R.L. Penn, S. Whitelam, D. Joester, H. Zhang, J.D. Rimer, A. Navrotsky, J.F. Banfield, A.F. Wallace, F.M. Michel, F.C. Meldrum, H. Cölfen, P.M. Dove, Crystallization by particle attachment in synthetic, biogenic, and geologic environments, Science. 349 (2015) aaa6760.

[6] F.A. Shah, K. Ruscsák, A. Palmquist, 50 years of scanning electron microscopy of bone—a comprehensive overview of the important discoveries made and insights gained into bone material properties in health, disease, and taphonomy, Bone Res. 7 (2019) 15.

[7] M. Georgiadis, R. Müller, P. Schneider, Techniques to assess bone ultrastructure organization: orientation and arrangement of mineralized collagen fibrils, J Roy Soc Interface. 13 (2016) 20160088.

[8] K. Grandfield, Bone, implants, and their interfaces, Phys Today. 68 (2015) 40–45.

[9] D.M. Binkley, K. Grandfield, Advances in Multiscale Characterization Techniques of Bone and Biomaterials Interfaces, Acs Biomater Sci Eng. 4 (2017) 3678–3690.

[10] M.L. Bouxsein, S.K. Boyd, B.A. Christiansen, R.E. Guldberg, K.J. Jepsen, R. Müller, Guidelines for assessment of bone microstructure in rodents using micro–computed tomography, J Bone Miner Res. 25 (2010) 1468–1486.

[11] N.K. Wittig, M. Østergaard, J. Palle, T.E.K. Christensen, B.L. Langdahl, L. Rejnmark, E.-M. Hauge, A. Brüel, J.S. Thomsen, H. Birkedal, Opportunities for biomineralization research using multiscale computed X-ray tomography as exemplified by bone imaging, J Struct Biol. 214 (2022) 107822.

[12] S. Weiner, E. Raguin, R. Shahar, High resolution 3D structures of mineralized tissues in health and disease, Nat Rev Endocrinol. 17 (2021) 307–316.

[13] N. Reznikov, R. Almany-Magal, R. Shahar, S. Weiner, Three-dimensional imaging of collagen fibril organization in rat circumferential lamellar bone using a dual beam electron microscope reveals ordered and disordered sub-lamellar structures, Bone. 52 (2013) 676–683.

[14] N. Reznikov, R. Shahar, S. Weiner, Three-dimensional structure of human lamellar bone: The presence of two different materials and new insights into the hierarchical organization, Bone. 59 (2014) 93–104.

[15] D.J. Buss, N. Reznikov, M.D. McKee, Crossfibrillar mineral tessellation in normal and Hyp mouse bone as revealed by 3D FIB-SEM microscopy, J Struct Biol. 212 (2020) 107603.

[16] D.J. Buss, R. Kröger, M.D. McKee, N. Reznikov, Hierarchical organization of bone in three dimensions: A twist of twists, J Struct Biology X. (2021) 100057.

[17] M.D. McKee, D.J. Buss, N. Reznikov, Mineral tessellation in bone and the stenciling principle for extracellular matrix mineralization, J Struct Biol. 214 (2022) 107823.

[18] D.M. Binkley, J. Deering, H. Yuan, A. Gourrier, K. Grandfield, Ellipsoidal mesoscale mineralization pattern in human cortical bone revealed in 3D by plasma focused ion beam serial sectioning, J Struct Biol. (2020) 107615.

[19] W.J. Landis, K.J. Hodgens, J. Arena, M.J. Song, B.F. McEwen, Structural relations between collagen and mineral in bone as determined by high voltage electron microscopic tomography, Microsc Res Techniq. 33 (1996) 192–202.

[20] E. McNally, F. Nan, G.A. Botton, H.P. Schwarcz, Scanning transmission electron microscopic tomography of cortical bone using Z-contrast imaging, Micron. 49 (2013) 46–53.

[21] N. Reznikov, M. Bilton, L. Lari, M.M. Stevens, R. Kröger, Fractal-like hierarchical organization of bone begins at the nanoscale, Science. 360 (2018) eaao2189.

[22] X. Wang, B. Langelier, F.A. Shah, A. Korinek, M. Bugnet, A.P. Hitchcock, A. Palmquist, K. Grandfield, Biomineralization at Titanium Revealed by Correlative 4D Tomographic and Spectroscopic Methods, Adv Mater Interfaces. 5 (2018) 1800262.

[23] B. Gault, A. Chiaramonti, O. Cojocaru-Mirédin, P. Stender, R. Dubosq, C. Freysoldt, S.K. Makineni, T. Li, M. Moody, J.M. Cairney, Atom probe tomography, Nat Rev Methods Primers. 1 (2021) 51.

[24] A.D. Giddings, S. Koelling, Y. Shimizu, R. Estivill, K. Inoue, W. Vandervorst, W.K. Yeoh, Industrial application of atom probe tomography to semiconductor devices, Scripta Mater. 148 (2018) 82–90.

[25] L.M. Gordon, D. Joester, Nanoscale chemical tomography of buried organic–inorganic interfaces in the chiton tooth, Nature. 469 (2011) 194--197.

[26] A. Pérez-Huerta, F. Laiginhas, Preliminary Data on the Nanoscale Chemical Characterization of the Inter-Crystalline Organic Matrix of a Calcium Carbonate Biomineral, Mineral-Basel. 8 (2018) 223.

[27] A. Pérez-Huerta, M. Suzuki, C. Cappelli, F. Laiginhas, H. Kintsu, Atom Probe Tomography (APT) Characterization of Organics Occluded in Single Calcite Crystals: Implications for Biomineralization Studies, C J Carbon Res. 5 (2019) 50.

[28] L.M. Gordon, M.J. Cohen, K.W. MacRenaris, J.D. Pasteris, T. Seda, D. Joester, Amorphous intergranular phases control the properties of rodent tooth enamel, Science. 347 (2015) 746–750.

[29] L.M. Gordon, D. Joester, Mapping residual organics and carbonate at grain boundaries and the amorphous interphase in mouse incisor enamel, Front Physiol. 6 (2015) 57.

[30] A.L. Fontaine, A. Zavgorodniy, H. Liu, R. Zheng, M. Swain, J. Cairney, Atomic-scale compositional mapping reveals Mg-rich amorphous calcium phosphate in human dental enamel, Sci Adv. 2 (2016) e1601145.

[31] F. Yun, M.V. Swain, H. Chen, J. Cairney, J. Qu, G. Sha, H. Liu, S.P. Ringer, Y. Han, L. Liu, X. Zhang, R. Zheng, Nanoscale pathways for human tooth decay – Central planar defect, organic-rich precipitate and high-angle grain boundary, Biomaterials. 235 (2020) 119748.

[32] O. Branson, E.A. Bonnin, D.E. Perea, H.J. Spero, Z. Zhu, M. Winters, B. Hönisch, A.D. Russell, J.S. Fehrenbacher, A.C. Gagnon, Nanometer-Scale Chemistry of a Calcite Biomineralization Template: Implications for Skeletal Composition and Nucleation, Proc National Acad Sci. 113 (2016) 12934–12939.

[33] K. Eder, L.M. Otter, L. Yang, D.E. Jacob, J.M. Cairney, Overcoming Challenges Associated with the Analysis of Nacre by Atom Probe Tomography, Geostand Geoanal Res. 43 (2019) 385–395.

[34] Y. Ren, H. Autefage, J.R. Jones, M.M. Stevens, P.A.J. Bagot, M.P. Moody, Developing Atom Probe Tomography to Characterize Sr-Loaded Bioactive Glass for Bone Scaffolding, Microsc Microanal. (2021) 1–11.

[35] L. Fu, J. Williams, C. Micheletti, B.E.J. Lee, G. Xu, J. Huang, H. Engqvist, W. Xia, K. Grandfield, Three-Dimensional Insights into Interfacial Segregation at the Atomic Scale in a Nanocrystalline Glass-Ceramic, Nano Lett. 21 (2021) 6898–6906.

[36] J. Karlsson, G. Sundell, M. Thuvander, M. Andersson, Atomically Resolved Tissue Integration, Nano Lett. 14 (2014) 4220–4223.

[37] M.K. Miller, R.G. Forbes, Atom-Probe Tomography, The Local Electrode Atom Probe, (2014) 51–109.

[38] B. Gault, M.P. Moody, J.M. Cairney, S.P. Ringer, Atom probe microscopy, Springer, New York NY, 2012.

[39] D.J. Larson, T.J. Prosa, R.M. Ulfig, B.P. Geiser, T.F. Kelly, Local Electrode Atom Probe Tomography, (2013).

[40] E.W. Müller, K. Bahadur, Field Ionization of Gases at a Metal Surface and the Resolution of the Field Ion Microscope, Phys Rev. 102 (1956) 624–631.

[41] E.W. Müller, Atoms Visualized, Sci Am. 196 (1957) 113–125.

[42] E.W. Müller, J.A. Panitz, S.B. McLane, The Atom-Probe Field Ion Microscope, Rev Sci Instrum. 39 (1968) 83–86.

[43] J.A. Panitz, The 10 cm Atom Probe, Rev Sci Instrum. 44 (1973) 1034–1038.

[44] A. Cerezo, T.J. Godfrey, G.D.W. Smith, Application of a position-sensitive detector to atom probe microanalysis, Rev Sci Instrum. 59 (1988) 862–866.

[45] D. Blavette, A. Bostel, J.M. Sarrau, B. Deconihout, A. Menand, An atom probe for three-dimensional tomography, Nature. 363 (1993) 432–435.

[46] T.F. Kelly, T.T. Gribb, J.D. Olson, R.L. Martens, J.D. Shepard, S.A. Wiener, T.C. Kunicki, R.M. Ulfig, D.R. Lenz, E.M. Strennen, E. Oltman, J.H. Bunton, D.R. Strait, First Data from a Commercial Local Electrode Atom Probe (LEAP), Microsc Microanal. 10 (2004) 373–383.

[47] E.E. Müller, Field desorption, Phys. Rev. 102 (1956) 618–624.

[48] D.R. Kingham, The post-ionization of field evaporated ions: A theoretical explanation of multiple charge states, Surf Sci. 116 (1982) 273–301.

[49] B. Gault, D. Haley, F. de Geuser, M.P. Moody, E.A. Marquis, D.J. Larson, B.P. Geiser, Advances in the reconstruction of atom probe tomography data, Ultramicroscopy. 111 (2011) 448–457.

[50] P. Fratzl, R. Weinkamer, Nature's hierarchical materials, Progress in Materials Science. (2007).

[51] L.E. Bertassoni, Dentin on the nanoscale: Hierarchical organization, mechanical behavior and bioinspired engineering, Dent Mater. 33 (2017) 637–649.

[52] J.-Y. Rho, L. Kuhn-Spearing, P. Zioupos, Mechanical properties and the hierarchical structure of bone, Med Eng Phys. 20 (1998) 92–102.

[53] P. Fratzl, H.S. Gupta, E.P. Paschalis, P. Roschger, Structure and mechanical quality of the collagen–mineral nano-composite in bone, J Mater Chem. 14 (2004) 2115–2123.

[54] S. Weiner, H.D. Wagner, The material bone: structure-mechanical function relations, Annu. Rev. Mater. Sci. (1998).

[55] N. Reznikov, R. Shahar, S. Weiner, Bone hierarchical structure in three dimensions, Acta Biomater. 10 (2014) 3815–3826.

[56] E.A. McNally, H.P. Schwarcz, G.A. Botton, A.L. Arsenault, A Model for the Ultrastructure of Bone Based on Electron Microscopy of Ion-Milled Sections, Plos One. 7 (2012) e29258.

[57] L.M. Gordon, L. Tran, D. Joester, Atom probe tomography of apatites and bone-type mineralized tissues, Acs Nano. 6 (2012) 10667--10675.

[58] B. Langelier, X. Wang, K. Grandfield, Atomic scale chemical tomography of human bone, Sci Rep. 7 (2017) srep39958.

[59] B.E.J. Lee, B. Langelier, K. Grandfield, Visualization of Collagen–Mineral Arrangement Using Atom Probe Tomography, Adv Biology. 5 (2021) 2100657.

[60] L. Gordon, D. Joester, S. Suram, K. Kaluskar, K. Rajan, Atom Probe Tomography of Organic/Inorganic Interfaces in Biominerals, Microsc Microanal. 18 (2012) 1608–1609.

[61] O. Licata, U. Guha, J.D. Poplawsky, N. Aich, B. Mazumder, Probing Heterogeneity in Bovine Enamel Composition through Nanoscale Chemical Imaging using Atom Probe Tomography, Arch Oral Biol. 112 (2020) 104682.

[62] K.A. DeRocher, P.J.M. Smeets, B.H. Goodge, M.J. Zachman, P.V. Balachandran, L. Stegbauer, M.J. Cohen, L.M. Gordon, J.M. Rondinelli, L.F. Kourkoutis, D. Joester, Chemical gradients in human enamel crystallites, Nature. 583 (2020) 66–71.

[63] P.J. Smeets, K. DeRocher, M.J. Zachman, B.H. Goodge, L.F. Kourkoutis, D. Joester, Atomic-Scale Characterization Reveals Core-Shell Structure of Enamel Crystallites, Microsc Microanal. 25 (2019) 1722–1723.

[64] J.-B. Forien, J. Uzuhashi, T. Ohkubo, K. Hono, L. Luo, H.P. Schwarcz, A.C. Deymier, C. Krywka, C. Fleck, P. Zaslansky, X-ray diffraction and in situ pressurization of dentine apatite reveals nanocrystal modulus stiffening upon carbonate removal, Acta Biomater. 120 (2021) 91–103.

[65] R.M.S. Schofield, J. Bailey, J.J. Coon, A. Devaraj, R.W. Garrett, M.S. Goggans, M.G. Hebner, B.S. Lee, D. Lee, N. Lovern, S. Ober-Singleton, N. Saephan, V.R. Seagal, D.M. Silver, H.E. Som, J. Twitchell, X. Wang, J.S. Zima, M.H. Nesson, The homogenous alternative to biomineralization: Zn- and Mn-rich materials enable sharp organismal “tools” that reduce force requirements, Sci Rep. 11 (2021) 17481.

[66] S.C.J. Loo, T. Moore, B. Banik, F. Alexis, Biomedical Applications of Hydroxyapatite Nanoparticles, Curr Pharm Biotechno. 11 (2010) 333–342.

[67] V. Uskoković, D.P. Uskoković, Nanosized hydroxyapatite and other calcium phosphates: Chemistry of formation and application as drug and gene delivery agents, J Biomed Mater Res Part B Appl Biomaterials. 96B (2011) 152–191.

[68] D.S. Mosiman, Y. Chen, L. Yang, B. Hawkett, S.P. Ringer, B.J. Mariñas, J.M. Cairney, Atom Probe Tomography of Encapsulated Hydroxyapatite Nanoparticles, Small Methods. 5 (2021) 2000692.

[69] N. Metoki, S.-I. Baik, D. Isheim, D. Mandler, D.N. Seidman, N. Eliaz, Atomically resolved calcium phosphate coating on a gold substrate, Nanoscale. 10 (2018) 8451–8458.

[70] W. Höland, V. Rheinberger, E. Apel, C. van ’t Hoen, M. Höland, A. Dommann, M. Obrecht, C. Mauth, U. Graf-Hausner, Clinical applications of glass-ceramics in dentistry, J Mater Sci Mater Medicine. 17 (2006) 1037–1042.

[71] L. Fu, H. Engqvist, W. Xia, Glass–Ceramics in Dentistry: A Review, Materials. 13 (2020) 1049.

[72] Z. Yang, H. Gu, G. Sha, W. Lu, W. Yu, W. Zhang, Y. Fu, K. Wang, L. Wang, TC4/Ag Metal Matrix Nanocomposites Modified by Friction Stir Processing: Surface Characterization, Antibacterial Property, and Cytotoxicity in Vitro, Acs Appl Mater Inter. 10 (2018) 41155–41166.

[73] Y. Jiang, J.L. Carvalho-de-Souza, R.C.S. Wong, Z. Luo, D. Isheim, X. Zuo, A.W. Nicholls, I.W. Jung, J. Yue, D.-J. Liu, Y. Wang, V.D. Andrade, X. Xiao, L. Navrazhnykh, D.E. Weiss, X. Wu, D.N. Seidman, F. Bezanilla, B. Tian, Heterogeneous silicon mesostructures for lipid-supported bioelectric interfaces, Nat Mater. 15 (2016) 1023–1030.

[74] M. Yan, M.S. Dargusch, T. Ebel, M. Qian, A transmission electron microscopy and three-dimensional atom probe study of the oxygen-induced fine microstructural features in as-sintered Ti–6Al–4V and their impacts on ductility, Acta Mater. 68 (2014) 196–206.

[75] J. Coakley, V.A. Vorontsov, N.G. Jones, A. Radecka, P.A.J. Bagot, K.C. Littrell, R.K. Heenan, F. Hu, A.P. Magyar, D.C. Bell, D. Dye, Precipitation processes in the Beta-Titanium alloy Ti–5Al–5Mo–5V–3Cr, J Alloy Compd. 646 (2015) 946–953.

[76] A. Devaraj, V.V. Joshi, A. Srivastava, S. Manandhar, V. Moxson, V.A. Duz, C. Lavender, A low-cost hierarchical nanostructured beta-titanium alloy with high strength, Nat Commun. 7 (2016) 11176.

[77] P.A.J. Bagot, A. Radecka, A.P. Magyar, Y. Gong, D.C. Bell, G.D.W. Smith, M.P. Moody, D. Dye, D. Rugg, The effect of oxidation on the subsurface microstructure of a Ti-6Al-4V alloy, Scripta Mater. 148 (2018) 24–28.

[78] J. Coakley, A. Radecka, D. Dye, P.A.J. Bagot, T.L. Martin, T.J. Prosa, Y. Chen, H.J. Stone, D.N. Seidman, D. Isheim, Characterizing nanoscale precipitation in a titanium alloy by laser-assisted atom probe tomography, Mater Charact. 141 (2018) 129–138.

[79] T.L. Martin, A. Radecka, L. Sun, T. Simm, D. Dye, K. Perkins, B. Gault, M.P. Moody, P.A.J. Bagot, Insights into microstructural interfaces in aerospace alloys characterised by atom probe tomography, Mater Sci Tech Ser. 32 (2016) 232–241.

[80] B. Gault, W. Yang, K.R. Ratinac, R. Zheng, F. Braet, S.P. Ringer, Atom Probe Microscopy of Self-Assembled Monolayers: Preliminary Results, Langmuir. 26 (2010) 5291–5294.

[81] A. Stoffers, C. Oberdorfer, G. Schmitz, Controlled Field Evaporation of Fluorinated Self-Assembled Monolayers, Langmuir. 28 (2012) 56–59.

[82] K. Eder, P.J. Felfer, B. Gault, A.V. Ceguerra, A.L. Fontaine, A.F. Masters, T. Maschmeyer, J.M. Cairney, A New Approach to Understand the Adsorption of Thiophene on Different Surfaces: An Atom Probe Investigation of Self-Assembled Monolayers, Langmuir. 33 (2017) 9573–9581.

[83] S.K. Mohanty, O. Tolochko, An atom probe analysis of self-assembled monolayers: A novel approach to investigate mixed and unmixed self-assembled monolayers (SAMs) on gold, Appl Surf Sci. 494 (2019) 152–161.

[84] T. Albrektsson, P.-I. Brånemark, H.-A. Hansson, J. Lindström, Osseointegrated Titanium Implants: Requirements for Ensuring a Long-Lasting, Direct Bone-to-Implant Anchorage in Man, Acta Orthop Scand. 52 (1981) 155–170.

[85] A. Palmquist, K. Grandfield, B. Norlindh, T. Mattsson, R. Brånemark, P. Thomsen, Bone–titanium oxide interface in humans revealed by transmission electron microscopy and electron tomography, J Roy Soc Interface. 9 (2012) 396–400.

[86] K. Grandfield, S. Gustafsson, A. Palmquist, Where bone meets implant: the characterization of nano-osseointegration, Nanoscale. 5 (2013) 4302–4308.

[87] F.A. Shah, P. Thomsen, A. Palmquist, Osseointegration and current interpretations of the bone-implant interface, Acta Biomater. 84 (2018) 1–15.

[88] G. Sundell, C. Dahlin, M. Andersson, M. Thuvander, The bone-implant interface of dental implants in humans on the atomic scale, Acta Biomater. 48 (2017) 445–450.

[89] J.-S. Kim, J.-P. Ahn, Y.-H. Kim, K.W. Seo, H. Zadeh, S.-H. Kim, Atomic layout of an orthodontic titanium mini-implant in human tissue:, Angle Orthod. 89 (2018) 292–298.

[90] D. Arola, S. Murcia, M. Stossel, R. Pahuja, T. Linley, A. Devaraj, M. Ramulu, E.A. Ossa, J. Wang, The limiting layer of fish scales: Structure and properties, Acta Biomater. 67 (2018) 319–330.

[91] A. Pérez-Huerta, F. Laiginhas, D.A. Reinhard, T.J. Prosa, R.L. Martens, Atom probe tomography (APT) of carbonate minerals, Micron. 80 (2016) 83–89.

[92] H. Kintsu, A. Pérez-Huerta, S. Ohtsuka, T. Okumura, S. Ifuku, K. Nagata, T. Kogure, M. Suzuki, Functional analyses of chitinolytic enzymes in the formation of calcite prisms in Pinctada fucata, Micron. 145 (2021) 103063.

[93] V.R. Adineh, R.K.W. Marceau, T. Velkov, J. Li, J. Fu, Near-Atomic Three-Dimensional Mapping for Site-Specific Chemistry of ‘Superbugs,’ Nano Lett. 16 (2016) 7113–7120.

[94] V.R. Adineh, C. Zheng, Q. Zhang, R.K.W. Marceau, B. Liu, Y. Chen, K.J. Si, M. Weyland, T. Velkov, W. Cheng, J. Li, J. Fu, Graphene-Enhanced 3D Chemical Mapping of Biological Specimens at Near-Atomic Resolution, Adv Funct Mater. 28 (2018) 1801439.

[95] K. Narayan, T.J. Prosa, J. Fu, T.F. Kelly, S. Subramaniam, Chemical mapping of mammalian cells by atom probe tomography, J Struct Biol. 178 (2012) 98–107.

[96] M.E. Greene, T.F. Kelly, D.J. Larson, T.J. Prosa, Focused ion beam fabrication of solidified ferritin into nanoscale volumes for compositional analysis using atom probe tomography, J Microsc-Oxford. 247 (2012) 288–299.

[97] D.E. Perea, J. Liu, J. Bartrand, Q. Dicken, S.T. Thevuthasan, N.D. Browning, J.E. Evans, Atom Probe Tomographic Mapping Directly Reveals the Atomic Distribution of Phosphorus in Resin Embedded Ferritin, Sci Rep. 6 (2016) 22321.

[98] S. Qiu, C. Zheng, V. Garg, Y. Chen, G. Gervinskas, J. Li, M.A. Dunstone, R.K.W. Marceau, J. Fu, Three-Dimensional Chemical Mapping of a Single Protein in the Hydrated State with Atom Probe Tomography, Anal Chem. 92 (2020) 5168–5177.

[99] K.A.K. Rusitzka, L.T. Stephenson, A. Szczepaniak, L. Gremer, D. Raabe, D. Willbold, B. Gault, A near atomic-scale view at the composition of amyloid-beta fibrils by atom probe tomography, Sci Rep. 8 (2018) 17615.

[100] G. Sundell, M. Hulander, A. Pihl, M. Andersson, Atom Probe Tomography for 3D Structural and Chemical Analysis of Individual Proteins, Small. 15 (2019) 1900316.

[101] O. Nishikawa, M. Taniguchi, A. Ikai, Atomic level analysis of biomolecules by the scanning atom probe, Appl Surf Sci. 256 (2009) 1210–1213.

[102] O. Nishikawa, M. Taniguchi, Toward the Atomic-Level Mass Analysis of Biomolecules by the Scanning Atom Probe, Microsc Microanal. 23 (2017) 336–339.

[103] F. Vurpillot, A. Bostel, D. Blavette, Trajectory overlaps and local magnification in three-dimensional atom probe, Appl Phys Lett. 76 (2000) 3127–3129.

[104] I. Arslan, E.A. Marquis, M. Homer, M.A. Hekmaty, N.C. Bartelt, Towards better 3-D reconstructions by combining electron tomography and atom-probe tomography, Ultramicroscopy. 108 (2008) 1579–1585.

[105] D.W. Saxey, S.M. Reddy, D. Fougerouse, W.D.A. Rickard, Microstructural Geochronology, Geophys Monogr Ser. (2017) 293–313.

[106] R. Verberne, D.W. Saxey, S.M. Reddy, W.D.A. Rickard, D. Fougerouse, C. Clark, Analysis of Natural Rutile (TiO2) by Laser-assisted Atom Probe Tomography, Microsc Microanal. 25 (2019) 539–546.

[107] A.J. London, D. Haley, M.P. Moody, Single-Ion Deconvolution of Mass Peak Overlaps for Atom Probe Microscopy, Microsc Microanal. 23 (2017) 300–306.

[108] K. Thompson, B. Gorman, D. Larson, B. van Leer, L. Hong, Minimization of Ga Induced FIB Damage Using Low Energy Clean-up, Microsc Microanal. 12 (2006) 1736–1737.

[109] D.J. Larson, D.T. Foord, A.K. Petford-Long, H. Liew, M.G. Blamire, A. Cerezo, G.D.W. Smith, Field-ion specimen preparation using focused ion-beam milling, Ultramicroscopy. 79 (1999) 287–293.

[110] M.K. Miller, K.F. Russell, G.B. Thompson, Strategies for fabricating atom probe specimens with a dual beam FIB, Ultramicroscopy. 102 (2005) 287–298.

[111] K. Thompson, D. Lawrence, D.J. Larson, J.D. Olson, T.F. Kelly, B. Gorman, In situ site-specific specimen preparation for atom probe tomography, Ultramicroscopy. 107 (2007) 131–139.

[112] D.J. Larson, T.J. Prosa, J.H. Bunton, D.P. Olson, D.F. Lawrence, E. Oltman, S.N. Strennin, T.F. Kelly, Improved Mass Resolving Power and Yield in Atom Probe Tomography, Microsc Microanal. 19 (2013) 994–995.

[113] F. Exertier, J. Wang, J. Fu, R.K.W. Marceau, Understanding the Effects of Graphene Coating on the Electrostatic Field at the Tip of an Atom Probe Tomography Specimen, Microsc Microanal. (2021) 1–12.

[114] S.S.A. Gerstl, R. Wepf, Methods in Creating, Transferring, & Measuring Cryogenic Samples for APT, Microsc Microanal. 21 (2015) 517–518.

[115] D.E. Perea, S.S.A. Gerstl, J. Chin, B. Hirschi, James.E. Evans, An environmental transfer hub for multimodal atom probe tomography, Adv Struct Chem Imaging. 3 (2017) 12.

[116] L.T. Stephenson, A. Szczepaniak, I. Mouton, K.A.K. Rusitzka, A.J. Breen, U. Tezins, A. Sturm, D. Vogel, Y. Chang, P. Kontis, A. Rosenthal, J.D. Shepard, U. Maier, T.F. Kelly, D. Raabe, B. Gault, The Laplace Project: An integrated suite for preparing and transferring atom probe samples under cryogenic and UHV conditions, Plos One. 13 (2018) e0209211.

[117] C. Macauley, M. Heller, A. Rausch, F. Kümmel, P. Felfer, A versatile cryo-transfer system, connecting cryogenic focused ion beam sample preparation to atom probe microscopy, Plos One. 16 (2021) e0245555.

[118] I.E. McCarroll, P.A.J. Bagot, A. Devaraj, D.E. Perea, J.M. Cairney, New frontiers in atom probe tomography: a review of research enabled by cryo and/or vacuum transfer systems, Mater Today Adv. 7 (2020) 100090.

[119] P. Stender, B. Gault, T.M. Schwarz, E.V. Woods, S.-H. Kim, J. Ott, L.T. Stephenson, G. Schmitz, C. Freysoldt, J. Kastner, A.A. El-Zoka, Status and direction of atom probe analysis of frozen liquids, ArXiv. (2021).

[120] Y.-S. Chen, M.J. Griffith, J.M. Cairney, Cryo Atom Probe: Freezing atoms in place for 3D mapping, Nano Today. 37 (2021) 101107.